Spin–Orbit Coupled Dynamics of Ferromagnetic Spinor Bose–Einstein Condensate

Qiang Zhao*

Department of Applied Physics, North China University of Science and Technology, Tangshan 063210, China

Received: 03.10.2023 & Accepted: 03.01.2024

Doi: 10.12693/APhysPolA.145.162 *e-mail: zhaoqiangac2004@sina.com

In this paper, we investigate the dynamic properties of spin–orbit coupling spin-1 ferromagnetic Bose–Einstein condensates with different trap geometry. Our results are obtained in terms of the three-component Gross–Pitaevskii equation of mean-field theory. Two kinds of trap potential are discussed: isotropic and anisotropic. It is shown that the spin-exchange dynamics are greatly influenced by trap geometry. For the latter with weak spin–orbit coupling strength, we find that the three-component oscillation accelerates and some small difference emerges between component $m = 1$ and $m = -1$. With the increase in spin–orbit coupling strength, the three components reach almost the same population. In addition, the kinetic energy of the system changes within a small scope for strong spin–orbit coupling, as opposed to a constant value in an isotropic trap. The density distributions display that the stripe phase appears with the increase in spin–orbit coupling strength. The method of generating stripe structure is different from the ground state of ferromagnetic condensate. For isotropic trap, the spatial separation of top and bottom spin–orbit condensates in component $m = 1$ and $m = -1$ occurs at weak spin–orbit coupling, and square lattice appears at strong spin–orbit coupling.

topics: stripe phase, dynamics process, spin–orbit coupled, spinor condensate

1. Introduction

The recent experimental realization of spin–orbit coupling (SOC) for boson [1, 2] and fermion [3, 4] ultracold quantum gases has stimulated much theoretical and experimental activity. The SOC is created by the synthetic non-Abelian gauge potentials, which provide a coupling between the center-of-mass motion and the internal degrees of freedom. This opens up possibilities of exploring exotic quantum matter characterizing magnetic and spin–orbit effects. A variety of interesting phenomena have been found in this subject, for instance, the stripe phase and vortex necklace in the ground states [5–9], twisted spin vortices [10], topological superfluidity [11] in fermionic gases, expansion of a Bose–Einstein condensate (BEC) [12] and Mott-insulating phases in optical lattice [13], and so on. For review properties of SOC in BEC, see [14, 15] and references therein.

On the other hand, the issue of trap geometry gained great attention in the field of BECs, and its role is intensively investigated. The mechanism of Josephson dynamics in the presence of interference between longitudinal and transversal fragmentation, produced by the geometry of the trap, is put forward in [16]. In [17], the authors display that the trap geometry and low temperature of the molecules decrease inelastic loss to ensure thermal equilibrium. As a result, colder and denser molecules can be prepared. In addition, the large-area ^{87}Rb BECs are created using a non-Gaussian optical dipole trap by adjusting the geometry structure of the trap [18]. In particular, Prasad et al. [19] theoretically demonstrate that the tilt angle of the stationary state body frame concerning the rotation axis is a non-trivial function of the trap geometry [19]. Moreover, they further show that the initial geometry can play an essential role in the focused scheme so that better resolutions and peak densities can be achieved by cylindrical BECs [20].

Very recently, phase separation has been one of the central research topics in the field of cold atom systems. It is extensively studied in BECs. By utilizing an inhomogeneous artificial gauge field, the condensate forms a localized vortex lattice structure that gives rise to a non-trivial symmetry breaking in the phase-separated regime [21]. The phase separation for a mixture of two interacting BECs under a magnetic field is studied [22]. Ota et al. [23] find that thermal fluctuation plays a significant role in the miscibility condition of a two-component mixture, favoring phase separation at a finite temperature, even if the mixture is soluble at zero temperature. It is reported that a two-dimensional (2D) SOC

can introduce an unconventional spatial separation in a trapped binary BEC with miscible interactions [24]. In addition, the Rayleigh–Taylor instability in a phase-separated three-component BEC is investigated [25].

It is quite a known fact that dynamical and ground states are two important aspects of characterizing physical nature, and the emphasis on them is different. The advantage of the dynamical state is that it shows the change of physical quantity in real-time. As a consequence, the dynamic procedure is well understood. Moreover, the ground state gives the final results and cannot show the variation processes. The motivation of this manuscript is to study the spin dynamics, the dynamical evolution of the kinetic energy, and the change in density structure. Therefore, we opt to investigate dynamical properties instead of examining the phase diagram or ground state. In this article, we study the spin-1 ferromagnetic BEC with 2D SOC trapped in a harmonic trap. The effects of SOC strength and different trap geometries are discussed.

The rest of the paper is organized in the following way. In Sect. 2, we formulate the theoretical models describing the SOC spin-1 BEC, and the details of the numerical method are given. In Sect. 3, the effects of the SOC and anisotropic trap potential on the dynamic properties of such a system are investigated. Finally, we present a brief conclusion in Sect. 4.

2. Theoretical model

We consider spin-1 BECs in a harmonic trap $V_{tr}(\boldsymbol{r}) = \frac{1}{2}M(\omega_x^2x^2 + \omega_y^2y^2 + \omega_z^2y^2)$, where ω_x, ω_y, and ω_z are the trap frequencies along the x, y, and z direction, respectively. The dilute BECs at zero temperature can be described by the mean-field Gross–Pitaevskii (GP) equation [26, 27],

$$\mathrm{i}\hbar\frac{\partial\psi_1}{\partial t} = \left[-\frac{\hbar^2}{2M}\nabla^2+V_{tr}+c_0\rho+c_2(\rho_1+\rho_0-\rho_{-1})\right]\psi_1 +c_2\psi_{-1}^*\psi_0^2 + \lambda\big(-\mathrm{i}\partial_x-\partial_y\big)\psi_0, \quad (1)$$

$$\mathrm{i}\hbar\frac{\partial\psi_0}{\partial t} = \left[-\frac{\hbar^2}{2M}\nabla^2 + V_{tr} + c_0\rho + c_2(\rho_1+\rho_{-1})\right]\psi_0 +2c_2\psi_{-1}\psi_0^*\psi_1+\lambda\big(-\mathrm{i}\partial_x+\partial_y\big)\psi_1 +\lambda\big(-\mathrm{i}\partial_x-\partial_y\big)\psi_{-1}, \quad (2)$$

$$\mathrm{i}\hbar\frac{\partial\psi_{-1}}{\partial t}= \left[-\frac{\hbar^2}{2M}\nabla^2 + V_{tr} + c_0\rho + c_2(\rho_{-1}+\rho_0-\rho_1)\right]\psi_{-1} +c_2\psi_1^*\psi_0^2 + \lambda\big(-\mathrm{i}\partial_x+\partial_y\big)\psi_0, \quad (3)$$

where $\psi_m(\boldsymbol{r})$ $(m = 1, 0, -1)$ is the field operator that annihilates an atom at point $\boldsymbol{r}$; $\rho_m = |\psi_m|^2$ is the density in the m-th hyperfine state; $\rho = \sum_m \rho_m$ is the total density normalized to the total number of atoms N; M is the atomic mass; λ is SOC strength. The coefficients $c_0 = \frac{4\pi N\hbar^2(a_0+2a_2)}{3M}$ and $c_2 = \frac{4\pi N\hbar^2(a_2-a_0)}{3M}$ describe binary elastic collisions in the channel of total spin 0 and 2 in terms of the s-wave scattering lengths a_0 and a_2.

In this work, we assume a transverse harmonic confinement. In the case of an oblate trap, the tight confinement $\omega_z \gg \omega_x$ and $\omega_z \gg \omega_y$ ensures that no excited states are available in the longitudinal z direction, and thus, the dynamics occur along the transverse direction x–y plane. Factorizing $\psi_m(\boldsymbol{r})$ into a longitudinal and a transverse function $\psi_m(\boldsymbol{r}, t) = \phi_m(x, y)w_{1\mathrm{D}}(z)$, with $w_{1\mathrm{D}}(z) = \left(\frac{M\omega_z}{\pi\hbar}\right)^{1/4} \mathrm{e}^{-M\omega_z z^2/(2\hbar)}$ denoting the one-dimensional (1D) ground state of the longitudinal oscillator. After integrating out the z coordinate, the GP equation becomes two-dimensional for the transverse wave functions and the dimensionless form is

$$\mathrm{i}\frac{\partial\phi_1}{\partial t}= \left[-\frac{1}{2}\nabla^2+V+\beta_n n+\beta_s(n_1+n_0-n_{-1})\right]\phi_1 +\beta_s\phi_{-1}^*\phi_0^2 + \kappa(-\mathrm{i}\partial_x-\partial_y)\phi_0, \quad (4)$$

$$\mathrm{i}\frac{\partial\phi_0}{\partial t}= \left[-\frac{1}{2}\nabla^2+V+\beta_n n+\beta_s\big(n_1+n_{-1}\big)\right]\phi_0 +2\beta_s\phi_{-1}\phi_0^*\phi_1+\kappa\big(-\mathrm{i}\partial_x+\partial_y\big)\phi_1 +\kappa\big(-\mathrm{i}\partial_x-\partial_y\big)\phi_{-1}, \quad (5)$$

$$\mathrm{i}\frac{\partial\phi_{-1}}{\partial t}= \left[-\frac{1}{2}\nabla^2+V+\beta_n n+\beta_s\big(n_{-1}+n_0-n_1\big)\right]\phi_{-1} +\beta_s\phi_1^*\phi_0^2 + \kappa\big(-\mathrm{i}\partial_x+\partial_y\big)\phi_0, \quad (6)$$

where $n = |\phi_1|^2+|\phi_0|^2+|\phi_{-1}|^2$, $V(x, y) = \frac{1}{2}(\gamma_x^2x^2+\gamma_y^2y^2)$, $\gamma_j = \omega_j/\omega$ $(j = x, y)$ with $\omega = \min\{\omega_x, \omega_y, \omega_z\}$, $\beta_n = \frac{2}{3}N(a_0+2a_2)\sqrt{\frac{\pi\omega M}{\hbar}}$, $\beta_s = \frac{2}{3}N(a_0-a_2)\sqrt{\frac{\pi\omega M}{\hbar}}$, $\kappa = \frac{\lambda NM}{2\hbar^2}\sqrt{\frac{M\omega}{\pi\hbar}}$. In our calculation, the units of length, time, energy, SOC strength, and wave function are $a_0 = \sqrt{\hbar/M\omega}, \omega^{-1}$, $\hbar\omega$, $\sqrt{\hbar\omega/M}$, and $a_0^{-3/2}$, respectively.

As for the numerical calculation, it consists of two parts. First, the ground state is generated by the imaginary time propagation with $m = 0$ and $\phi_{\pm1} = 0$. Then, the dynamics process is created by evolving the ground state with the initial fractions $(0.003, 0.994, 0.003)$ for three components in real-time propagation. Specifically, the time evolution is performed successively using the time-splitting Fourier spectral method [28, 29], i.e.,

$$\mathrm{i}\partial_t\phi_m = H_{\mathrm{KE}}\phi_m, \quad (7)$$

$$\mathrm{i}\partial_t\phi_m = H_{\mathrm{SOC}}\phi_m, \quad (8)$$

$$\mathrm{i}\partial_t\phi_m = H_{\mathrm{SP}}\phi_m, \quad (9)$$

where the kinetic energy operator $H_{\rm KE}$, spin–orbit coupling $H_{\rm SOC}$, and trap potential plus terms resulting from spin-preserving collisions $H_{\rm SP}$ are defined as

$$\hat{H}_{\rm KE} = \frac{1}{2}\begin{pmatrix} \mu_x^2+\mu_y^2 & 0 & 0 \\ 0 & \mu_x^2+\mu_y^2 & 0 \\ 0 & 0 & \mu_x^2+\mu_y^2 \end{pmatrix}, \tag{10}$$

$$\hat{H}_{\rm SOC} = \kappa\begin{pmatrix} 0 & \mu_x - \mathrm{i}\mu_y & 0 \\ \mu_x+\mathrm{i}\mu_y & 0 & \mu_x-\mathrm{i}\mu_y \\ 0 & \mu_x+\mathrm{i}\mu_y & 0 \end{pmatrix}, \tag{11}$$

and

$$H_{\rm SP} = \begin{pmatrix} V+\beta_n n+\beta_s(n_1+n_0-n_{-1}) & \beta_s\phi_0\phi_{-1}^* & 0 \\ \beta_s\phi_0^*\phi_{-1} & V+\beta_n n+\beta_s(n_1+n_{-1}) & \beta_s\phi_0^*\phi_1 \\ 0 & \beta_s\phi_0{\phi_1}^* & V+\beta_n n+\beta_s(n_0+n_{-1}-n_1) \end{pmatrix}. \tag{12}$$

Here, we give the expressions of $H_{\rm KE}$ and $H_{\rm SOC}$ in Fourier space $\hat{H}_{\rm KE}$ and $\hat{H}_{\rm SOC}$; μ_x and μ_y are known as Fourier frequency. Numerically, the matrixes are solved using the exact diagonalization method by the Lapack library [30]. The 2D spatial step and time step applied in the present manuscript are 0.125 and 0.001, respectively.

3. Results and discussion

In this article, we consider $N = 10^5$ spin-1 ferromagnetic ^{87}Rb atoms, which have $a_0 = 101.8a_{\rm B}$ and $a_2 = 101.4a_{\rm B}$ [31], where $a_{\rm B}$ is the Bohr radius. We consider two different trap potentials, i.e., isotropic and anisotropic. The trap frequencies for the former and latter are $\omega_{x,y,z} = 2\pi\times(10,10,150)$ Hz and $\omega_{x,y,z} = 2\pi\times(20,10,150)$ Hz, respectively. In this case, the dimensionless interaction strengths are $\beta_n = 3037.88$ and $\beta_s = -14.05$, and the units of length and time are $a_0 = 3.41$ μm and $\omega^{-1} = 1.59\times10^{-2}$ s. The aspect ratio in the quasi-2D regime is $\gamma_{x,y} = (1,1)$ and $\gamma_{x,y} = (2,1)$. For the sake of simplicity of notation, we denote them as $\gamma_{1,1}$ and $\gamma_{2,1}$. In addition, the dimensionless variables are shown in the rest of this paper unless mentioned otherwise.

We first investigate the populations of spin components for different SOC strengths and aspect ratios. Figure 1a shows the coherent oscillation for SOC strength $\lambda = 0.6$ and aspect ratio $\gamma_{1,1}$. The initially empty components $m = \pm1$ to develop, and the $m = \pm1$ components display nearly the same dynamical behavior. As SOC strength is increased to $\lambda = 0.8$ in Fig. 1b, the $m = \pm1$ and $m = 0$ components gradually increase and decrease and then reach a steady value. In this process, the $m = \pm1$ components still have the same dynamical behavior. Note that similar oscillation is also seen in [32], where the spin dynamics of antiferromagnetic atoms ^{23}Na condensate is studied. This fact reflects that such oscillation mode can exist independent of the magnetic phase (ferromagnetic $\beta_s < 0$ or antiferromagnetic $\beta_s > 0$) just by the use of a relatively strong SOC strength. As for the side of aspect ratio $\gamma_{2,1}$ in Fig. 1c, it is obvious that the oscillation speeds up. The peak of populations N_m/N appears alternately for components $m = 0$ and $m = \pm1$. Moreover, it is worth mentioning that $m = \pm1$ components present some small differences. When the SOC strength is gradually increased to $\lambda = 0.8$ in Fig. 1d, the fluctuation of spin components becomes small. As a result, the three components reach roughly equal populations.

The amount of kinetic energy is an important physical quantity for the dynamics process as it reflects the thermalization degree of the system. A stable spatial configuration is obtained when the kinetic energy achieves a steady value. In the work [33], the change in kinetic energy in spin-1 dipolar ferromagnetic ^{87}Rb condensate is shown at different trap geometries [33]. Here, we consider this issue for different SOC strengths. Figure 2a displays the kinetic energy in quasi-2D trap potential $\gamma_{1,1}$ as a function of time at $\lambda = 0.5, 0.6, 0.7, 0.8$, which is represented by the black, red, blue, and green lines, respectively. It is clear that the variation of kinetic energy is very small for weak SOC $\lambda = 0.5, 0.6$. As SOC strength is increased to $\lambda = 0.7$, the kinetic energy increases with non-periodic oscillation and gradually becomes stable. As SOC is further increased to $\lambda = 0.8$, the kinetic energy abruptly increases and then reaches a constant value. For the aspect ratio $\gamma_{2,1}$, the weak SOC $\lambda = 0.5, 0.6$ presents almost the same dynamic behavior as the case of $\gamma_{1,1}$, and the kinetic energy remains almost unchanged. Nevertheless, the thermalization time is greatly reduced at $\lambda = 0.7$. As a consequence, the kinetic energy quickly tends to level off after a short time oscillation, whereas the oscillation sustains for some time at $\lambda = 0.8$, and it is easy to see that

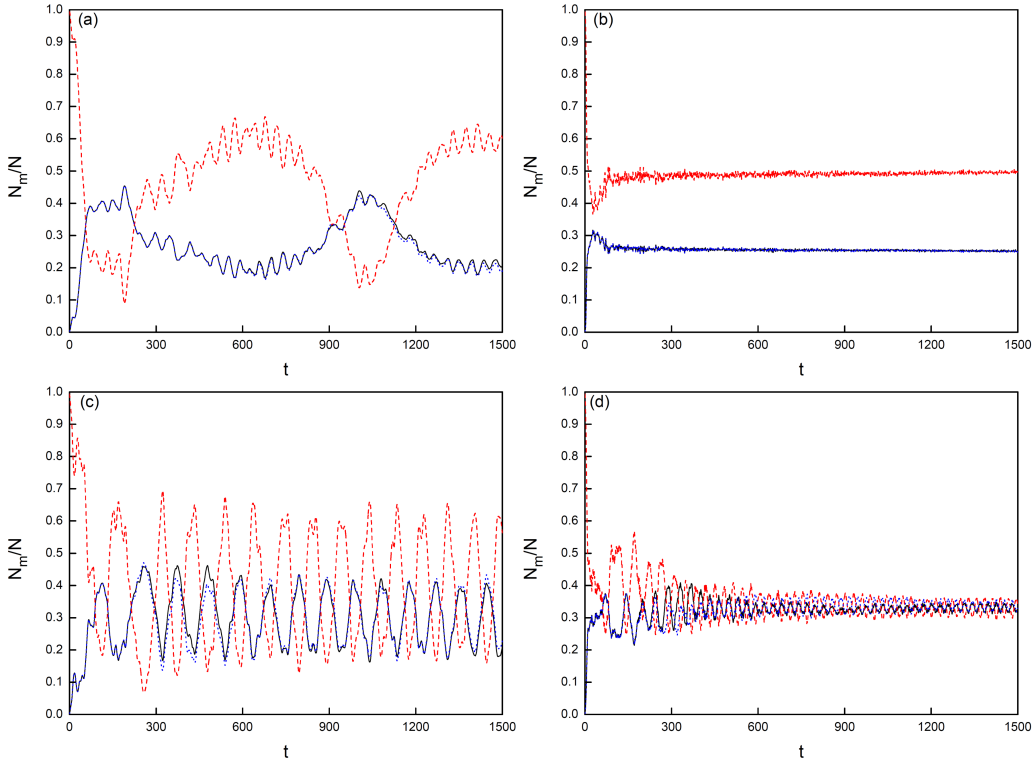

Fig. 1. Populations of spin components N_m/N as a function of time t. The black, red, and blue lines represent $m = 1, 0, -1$ components, respectively, with (a) $\lambda = 0.6$, $\gamma_{1,1}$, (b) $\lambda = 0.8$, $\gamma_{1,1}$, (c) $\lambda = 0.6$, $\gamma_{2,1}$, (d) $\lambda = 0.8$, $\gamma_{2,1}$. Simulation parameters: $c_0 = 3037.88$, $c_2 = -14.05$.

the degree of oscillation is very small. This point is different from the trap potential $\gamma_{1,1}$. Moreover, we verify that a stable spatial structure can be obtained in this case.

To get a more intuitive insight into the influence of the aspect ratio, we investigate the density profiles for three different components. Figure 3 shows the time evolution of the density profile at different SOC strengths. At $t = 300$ (first column), densities indicate that the $m = 0$ component is located on the central part, the $m = 1$ component occupies the top half, and the $m = -1$ component occupies the bottom half of the condensates. These occupations remain almost unchanged on a time scale such as $t = 1200$ (second column). The density structure for components $m = 1$ and $m = -1$ is complementary. Namely, the component $m = 1$ is located in the minimum density of component $m = -1$ and vice versa. We note that the spatial separation of top and bottom spin–orbit condensates is also observed in [34], where the ground state density configurations of pseudospin-1/2 SOC BECs are studied. With the increase in SOC strength, the square lattice is shown (third column), and this pattern is nearly the same at a finite time (fourth column). However, for antiferromagnetic condensate, unlike in the ferromagnetic case, the ground state density structure is a stripe pattern [5]. In addition, we also see that the complementarity exists for components $m = 1$ and $m = -1$.

The spatial density configurations corresponding to the aspect ratio $\gamma_{2,1}$ are shown in Fig. 4. It is observed that the density distribution for $\lambda = 0.6$ (first column) is similar to the case of $\gamma_{1,1}$ in Fig. 3 (first column). As time proceeds, the density distributions for $m = \pm 1$ component reverse (second column). Component $m = 1$ occupies the bottom half, while component $m = -1$ is on the top half of the condensates. When the SOC strength is increased to $\lambda = 0.8$, to our surprise, one can see that the stripe phase appears (third column). As mentioned earlier, the stripe phase is a key feature of the ground state of antiferromagnetic condensate. Furthermore, the stripe phase persists for a longer time (fourth column). Therefore, we deduce that the aspect ratio tends to create a stripe phase in the ferromagnetic condensate. It is worth mentioning that such a mechanism is not demonstrated in spin-1 condensate of ^{87}Rb. We stress that the relatively strong SOC strength is necessary for the generation of the stripe phase, and the complementarity still holds.

Finally, we give the experimental feasibility of the above analysis. In the ultracold quantum gas experiment, the ferromagnetic spinor BECs are prepared in rubidium vapor [35]. In this case, the interatomic interactions can be approximated by a short-range two-body potential, where the s-wave scattering length is the only relevant parameter. The SOC originates from the laser-assisted coupling

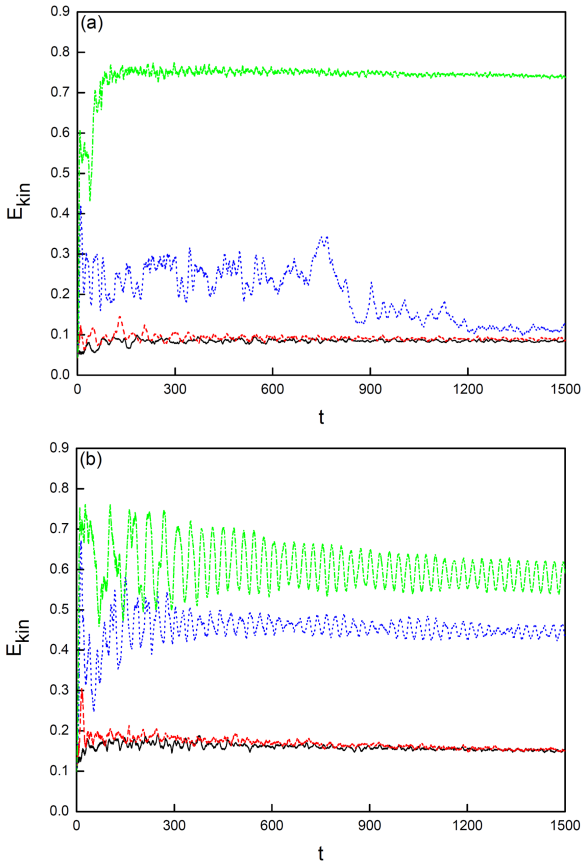

Fig. 2. Dynamical evolution of the kinetic energy E_{kin} with respect to time t with (a) $\gamma_{1,1}$, (b) $\gamma_{2,1}$. The black, red, blue, and green lines represent the SOC strength $\lambda = 0.5, 0.6, 0.7, 0.8$, respectively. Simulation parameters: $c_0 = 3037.88$, $c_2 = -14.05$.

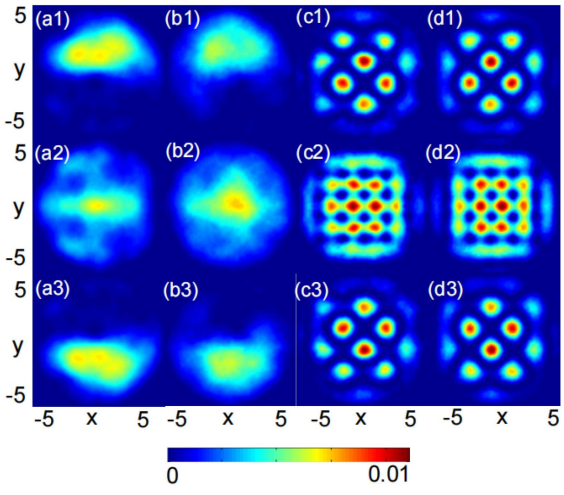

Fig. 3. Sequence of images of the density for the SOC spin-1 ^{87}Rb atoms with isotropic trap $\gamma_{1,1}$ for (a) $t = 300$, $\lambda = 0.6$, (b) $t = 1200$, $\lambda = 0.6$, (c) $t = 300$, $\lambda = 0.8$, (d) $t = 1200$, $\lambda = 0.8$. From top to bottom, the rows represent n_1, n_0, and n_{-1}. The area of view in the panels is $5a_0 \times 5a_0$. Simulation parameters: $c_0 = 3037.88$, $c_2 = -14.05$.

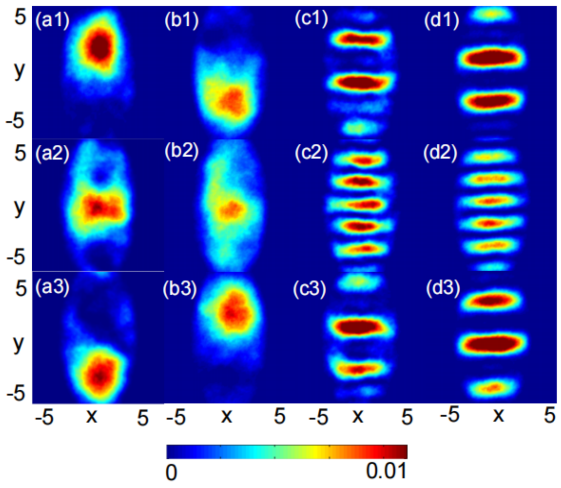

Fig. 4. Sequence of images of the density for the SOC spin-1 ^{87}Rb atoms with anisotropic trap $\gamma_{2,1}$ for (a) $t = 300$, $\lambda = 0.6$, (b) $t = 1200$, $\lambda = 0.6$, (c) $t = 300$, $\lambda = 0.8$, (d) $t = 1200$, $\lambda = 0.8$. From top to bottom, the rows represent n_1, n_0, and n_{-1}. The area of view in the panels is $5a_0 \times 5a_0$. Simulation parameters: $c_0 = 3037.88$, $c_2 = -14.05$.

between the atomic center-of-mass motion and the internal degrees of freedom, and it is realized in 2D form [36] and becomes a tunable resource [37]. As for the density structure, it can be directly observed by measuring the absorption image after free expansion [38]. In addition, the aspect ratio is easily adjusted by manipulating the trap frequency. It has been shown that the trap geometry issue has been widely discussed in recent years [39, 40]. We point out that the discussions above are confined to isotropy SOC strength. Anisotropic SOC strength plays a significant role in the formation of density distribution. We state that only a zero magnetic field is considered in the current manuscript, and it is estimated that the non-zero magnetic field has a great effect on the dynamics evolution process. Moreover, we note that much attention has been paid to mass imbalance in Bose and Fermi systems [41, 42], which generate rich physical phenomena. Some open questions can be explored in the future.

4. Conclusions

In conclusion, we have studied the dynamic properties of SOC spin-1 ferromagnetic BECs with different trap geometries. We found that the spin dynamics are seriously affected by the aspect ratio. Compared with the case of isotropic trap $\gamma_{1,1}$, for weak SOC strength, the populations in anisotropic trap $\gamma_{2,1}$ show that the three-component oscillation speeds up and some small difference occurs between component $m = 1$ and $m = -1$. With the increase in SOC strength, the three components

reach roughly equal populations. In addition, for the considered maximum SOC strength, the kinetic energy of the system changes within a narrow range, as opposed to a constant value for the isotropic trap. The density structures show that for the anisotropic trap, the stripe phase emerges with the increase in SOC strength. This mechanism for the creation of a stripe pattern is different from the ground state of ferromagnetic condensate. For isotropic trap, the spatial separation of top and bottom spin–orbit condensates in component $m = 1$ and $m = -1$ occurs at weak SOC, and square lattice appears at strong SOC strength.

Acknowledgments

This work is supported by the Innovation Fund of North China University of Science and Technology (Grant No. X2022266).

References

[1] Y.J. Lin, K. Jiménez-García, I.B. Spielman, *Nature* **471**, 83 (2011).

[2] J.Y. Zhang, S.C. Ji, Z. Chen et al., *Phys. Rev. Lett.* **109**, 115301 (2012).

[3] P. Wang, Z.Q. Yu, Z. Fu, J. Miao, L. Huang, S. Chai, H. Zhai, J. Zhang, *Phys. Rev. Lett.* **109**, 095301 (2012).

[4] L.W. Cheuk, A.T. Sommer, Z. Hadzibabic, T. Yefsah, W.S. Bakr, M.W. Zwierlein, *Phys. Rev. Lett.* **109**, 095302 (2012).

[5] C. Wang, C. Gao, C.M. Jian, H. Zhai, *Phys. Rev. Lett.* **105**, 160403 (2010).

[6] Z.F. Xu, R. Lü, L. You, *Phys. Rev. A* **83**, 053602 (2011).

[7] W. Han, G. Juzeliūnas, W. Zhang, W.M. Liu, *Phys. Rev. A* **91**, 013607 (2015).

[8] T. Ozawa, G. Baym, *Phys. Rev. A* **85**, 013612 (2012).

[9] T. Ozawa, G. Baym, *Phys. Rev. A* **85**, 063623 (2012).

[10] M. Kato, X.F. Zhang, D. Sasaki, H. Saito, *Phys. Rev. A* **94**, 043633 (2016).

[11] X.J. Liu, H. Hu, *Phys. Rev. A* **88**, 023622 (2013).

[12] M.A. Khamehchi, K. Hossain, M.E. Mossman, Y.P. Zhang, Th. Busch, M.M. Forbes, P. Engels, *Phys. Rev. Lett.* **118**, 155301 (2017).

[13] Z. Chen, Z. Liang, *Phys. Rev. A* **93**, 013601 (2016).

[14] H. Zhai, *Int. J. Mod. Phys. B* **26**, 1230001 (2012).

[15] H. Zhai, *Rep. Progr. Phys.* **78**, 026001 (2015).

[16] A. Bhowmik, O.E. Alon, arXiv:2207.05513 (2022).

[17] Z.D. Zhang, L.C. Chen, K.X. Yao, C. Chin, *Nature* **592**, 708 (2021).

[18] Y.H. Lim, J.H. Goo, H. Kwak, Y. Shin, *Phys. Rev. A* **103**, 063319 (2021).

[19] S.B. Prasad, B.C. Mulkerin, A.M. Martin, *Phys. Rev. A* **103**, 033322 (2021).

[20] R. Richberg, A.M. Martin, *Phys. Rev. A* **104**, 063306 (2021).

[21] S.S.S. Hejazi, J. Polo, R. Sachdeva, Th. Busch, *Phys. Rev. A* **102**, 053309 (2020).

[22] S.S. Aksu, A.L. Subaşı, N. Ghazanfari, *J. Phys. B* **54**, 045301 (2021).

[23] M. Ota, S. Giorgini, *Phys. Rev. A* **102**, 063303 (2020).

[24] Z.Q. Gui, Z.M. Zhang, J. Su, H. Lyu, Y.P. Zhang, *Phys. Rev. A* **108**, 043311 (2023).

[25] A. Saboo, S. Halder, S. Das, S. Majumder, *Phys. Rev. A* **108**, 013320 (2023).

[26] J. Mur-Petit, M. Guilleumas, A. Polls, A. Sanpera, M. Lewenstein, *Phys. Rev. A* **73**, 013629 (2006).

[27] T. Świsłocki, M. Matuszewski, *Phys. Rev. A* **85**, 023601 (2012).

[28] P. Kaur, A. Roy, S. Gautam, *Comput. Phys. Commun.* **259**, 107671 (2021).

[29] P. Banger, P. Kaur, A. Roy, S. Gautam, *Comput. Phys. Commun.* **279**, 108442 (2022).

[30] E. Anderson, Z. Bai, C. Bischof, S. Blackford, J. Demmel, J. Dongarra, J. Du. Croz, A. Greenbaum, S. Hammarling, A. McKenney, D. Sorensen, LAPACK Users Guide, SIAM, 1999.

[31] E.G.M. van Kempen, S.J.J.M.F. Kokkelmans, D.J. Heinzen, B.J. Verhaar, *Phys. Rev. Lett.* **88**, 093201 (2002).

[32] Q. Zhao, H.J. Bi, X.M. Yang, L.L. Zhang, *Int. J. Mod. Phys. B* **36**, 2250050 (2022).

[33] T. Świsłocki, M. Brewczyk, M. Gajda, K. Rzążewski, *Phys. Rev. A* **81**, 033604 (2010).

[34] J. Radić, T.A. Sedrakyan, I.B. Spielman, V. Galitski, *Phys. Rev. A* **84**, 063604 (2011).

[35] B.P. Anderson, M.A. Kasevich, *Science* **282**, 1686 (1998).

[36] L. Huang, Z. Meng, P. Wang, P. Peng, S.L. Zhang, L. Chen, D. Li, Q. Zhou, J. Zhang, *Nat. Phys.* **12**, 540 (2016).

[37] K. Jiménez-García, L.J. LeBlanc, R.A. Williams, M.C. Beeler, C. Qu, M. Gong, C. Zhang, I.B. Spielman, *Phys. Rev. Lett.* **114**, 125301 (2015).

[38] D. Wang, B. Neyenhuis, M.H.G. de Miranda, K.K. Ni, S. Ospelkaus, D.S. Jin, J. Ye, *Phys. Rev. A* **81**, 061404(R) (2010).

[39] J.P. Corson, R.M. Wilson, J.L. Bohn, *Phys. Rev. A* **88**, 013614 (2013).

[40] A.L. Subaşı, M. Iskin, *Phys. Rev. A* **105**, 023301 (2022).

[41] B. Parajuli, D. Pęcak, C.C. Chien, *Phys. Rev. A* **100**, 063623 (2019).

[42] A.D. Kerin, A.M. Martin, *Phys. Rev. A* **106**, 053310 (2022).